Carbon 230 (2024) 119613

Contents lists available at ScienceDirect

Carbon

journal homepage: www.elsevier.com/locate/carbon

Enhanced microwave absorption using multiple heterostructures derived from in-situ grown Sn-metal-organic framework on La-doped Fe_3O_4

Huiliang Wen [a], Wei Xu [b], Sen Lin [a], Aiguo Guan [c,*], Yingna Zhang [d], Xin Li [d], Chongbo Liu [d,**]

[a] School of New Energy Industry, Jiangxi Hongzhou Vocational College, Fengcheng, 331100, PR China
[b] Innovation and Entrepreneurship College, Jiangxi Hongzhou Vocation College, Fengcheng, 331100, PR China
[c] Jiangxi Hongzhou Vocational College, Fengcheng, 331100, PR China
[d] School of Environmental and Chemical Engineering, Nanchang Hangkong University, Nanchang, 330063, PR China

ARTICLE INFO

Keywords:
La-doped Fe_3O_4
3d-4f coupling
Sn-MOF
Enhanced microwave absorption
Multiple heterostructures

ABSTRACT

As a representative magnetic oxide absorber, Fe_3O_4 has attracted considerable research attention owing to its remarkable magnetic saturation strength as well as semiconducting properties. Doping Fe_3O_4 with La^{3+} leads to 3d-4f magnetic coupling and ion distribution changes due to the unique electron configuration and large ionic radius of La^{3+}, thereby greatly enhancing the magnetic performance. However, high density, low dielectric loss, and low permeability at high frequencies inhibit the electromagnetic wave absorption (EMWA) performance of ferrites. In this study, stick-shaped Sn metal-organic framework (MOF) is in-situ grown on La^{3+}-doped Fe_3O_4 using a surfactant. After high-temperature annealing, the SnO_2/porous carbon composites derived from Sn-MOF wrap the ferrite, forming a core-shell heterostructure, which not only prevents oxidation but also enhances the EMWA performance. Among the prepared $La_xFe_{3-x}O_4/SnO_2/C$ (LFSC) samples, LFSC-2 (with $La_xFe_{3-x}O_4$ to Sn-MOF ratio of 1:2) exhibits strong absorption performance with a minimum reflection loss (RL_{min}) of −44.1 dB. Furthermore, the gradient metamaterial based on LFSC-3 shows ultra-broadband EMWA with an effective absorption bandwidth ($RL_{min} \leq -10$ dB) of 13.17 GHz. In addition, the LFSC-2 sample demonstrates excellent radar stealth capability in the radar cross section (RCS) far-field response, achieving an RCS reduction value of 20.4 dB•m^2.

1. Introduction

The rapid development of modern electronic information technology, especially the advent of sixth-generation (6G) wireless communication, has brought great convenience to our daily life. However, this advancement has also caused serious electromagnetic (EM) pollution issues. EM radiation not only threatens human health but also interferes with the normal operation of precision instruments [1,2]. In addition, military equipment are coated with electromagnetic wave absorption (EMWA) materials to absorb radar waves and improve combat capability. Therefore, to address the environmental pollution issues and meet the military equipment demands, the development of effective EMWA materials has garnered considerable interest [3,4].

Due to its environmental friendliness, simple manufacturing process, and high saturation magnetization, Fe_3O_4 is widely used in the fields of permanent magnetism and EMWA. Du et al. proposed an environmentally friendly method for recovering iron from nickel slag, where iron was oxidized in the molten state to form Fe_3O_4, which was then obtained by magnetic separation. Fe_3O_4 achieved a minimum reflection loss (RL_{min}) of −29.90 dB and an effective absorption band (*EAB*, $RL_{min} \leq -10$ dB) at 3.28 GHz [5]. Further, doping magnetic oxides with La^{3+} leads to 3d-4f magnetic coupling, which is conducive to improving their magnetic properties. Hou et al. investigated the effect of Ce^{4+} doping in Fe_4N (Fe_4N/Ce) on the EMWA properties of Fe_4N. The electron migration polarization caused by Ce^{4+} combined with the excellent magnetic loss provided by the Fe_4N core resulted in an optimal EMWA performance. The *EAB* of Fe_4N/Ce reached 7.5 GHz at 1.5-mm thickness, while that of undoped Fe_4N was 5.6 GHz, proving that Ce^{4+} doping greatly enhanced EMWA performance of Fe_4N [6].

Although $La_xFe_{3-x}O_4$ exhibits high magnetic loss capacity, the low dielectric response limits its EMWA performance. Porous carbon materials show immense promise in EMWA application due to their ultralow

* Corresponding author.
** Corresponding author.
E-mail addresses: 275919486@qq.com (A. Guan), cbliu2002@163.com (C. Liu).

https://doi.org/10.1016/j.carbon.2024.119613
Received 8 July 2024; Received in revised form 28 August 2024; Accepted 7 September 2024
Available online 7 September 2024

density and excellent dielectric loss ability. Further, the unique porous structure can effectively reduce the effective permittivity (ε_{eff}) and further optimize the impedance matching. Ji et al. prepared porous carbon aerogel derived from Shaddock peel through freeze-drying and subsequent heat treatment. The numerous cavities inside the porous carbon aerogel increased the number of dipoles and dipole polarization, while its high porosity contributed to its lightweight characteristics. Consequently, the synthesized porous carbon aerogel achieved an effective bandwidth of 5.80 GHz at a thickness of only 1.7 mm [7]. Additionally, the porous carbon/metal or metal oxide composites, obtained by thermal reduction of metal-organic frameworks (MOFs), can significantly dissipate EMWs and hold great potential for EMWA application [8–10]. Liu et al. in-situ grew MOF-74 on NiFe to address the poor EMWA performance of NiFe. After calcination, the MOF-derived carbon enhanced the dielectric loss capability of the material, optimizing the impedance matching and ultimately improving the EMWA performance, with an *EAB* of 5.09 GHz [11].

In this study, we utilize the electrostatic adsorption strategy to in-situ grow stick-like Sn-MOF on $La_xFe_{3-x}O_4$. The stick-like morphology of Sn-MOF provides a special aspect ratio and high anisotropy, beneficial to the attenuation of electromagnetic waves (EMWs). After calcination, the derived porous carbon facilitates multiple reflections and scattering of EMWs. As an n-type semiconductor, SnO_2 can reduce the surface eddy currents of magnetic particles, enhancing the magnetic loss capability. Zhang et al. successfully synthesized Ni/SnO_2 composites with a core-shell structure by hydrothermal deposition, which exhibited excellent EMWA properties, with an RL_{min} of −42.8 dB at a thickness of 3.0 mm [12].

Here, the $La_xFe_{3-x}O_4/SnO_2$/C sample is first prepared using $La_xFe_{3-x}O_4$@Sn-MOF as the precursor. The unique 3d-4f coupling of La and Fe greatly enhances the magnetic saturation. After pyrolysis, the stick-like Sn-MOF-derived porous carbon and SnO_2 are tightly wrapped around the $La_xFe_{3-x}O_4$ core, resulting in a core-shell heterostructure. Thus, the special combination of $La_xFe_{3-x}O_4$ and Sn-MOF can effectively enhance the EMWA performance of conventional magnetic materials.

2. Experimental section

2.1. Materials

$FeCl_3•6H_2O$, $La(NO_3)_3•6H_2O$, $SnSO_4$, glycol, urea, cetyltrimethylammonium bromide (CTAB), polyvinylpyrrolidone, terephthalic acid, and N–N dimethylformamide (DMF) were purchased from Aladdin (Shanghai, China).

2.2. Synthesis of $La_xFe_{3-x}O_4$

Firstly, 2.75 g of $FeCl_3•6H_2O$, 0.0433 g of $La(NO_3)_3•6H_2O$, and 0.2 g of PVP were dissolved in 40 mL of ethylene glycol to obtain solution A. The solution was sonicated for 30 min before adding 1.2 g of urea, followed by another 10-minn sonication. The resulting uniform orange solution was transferred to a 100 mL polytetrafluoroethylene-lined vessel and maintained at 200 °C for 21 h. The resulting products were washed with deionized water and absolute ethanol, collected by centrifugation, and dried at 60 °C for 12 h. By varying the content of La^{3+}, different $La_xFe_{3-x}O_4$ samples (x = 0, 0.03, and 0.09) were prepared.

2.3. Synthesis of $La_xFe_{3-x}O_4$@Sn-MOF

Taking $La_{0.03}Fe_{2.97}O_4$@Sn-MOF (1:2) as an example, according to the classical synthesis steps [13], 0.075 g of $La_{0.03}Fe_{2.97}O_4$ and 0.075 g of CTAB were added to 1.5 mL of DMF and 1.5 mL of deionized water. The mixture was then sonicated for 10 min to obtain solution B. Subsequently, 0.1 g of terephthalic acid, 0.05 g of $Li(OH)_2•H_2O$, 0.161 g of $SnSO_4$, and 0.5 mL of deionized water were added to solution B and stirred for 2 h. The resulting products were washed with DMF and deionized water, then dried to obtain $La_{0.03}Fe_{2.97}O_4$@Sn-MOF with a $La_{0.03}Fe_{2.97}O_4$ to Sn-MOF ratio of 1:2. The $La_{0.03}Fe_{2.97}O_4$@Sn-MOF samples with $La_{0.03}Fe_{2.97}O_4$ to Sn-MOF ratios of 1:1 and 1:3 were prepared using the same method.

2.4. Synthesis of $La_{0.03}Fe_{2.97}O_4$@SnO_2/C

The $La_{0.03}Fe_{2.97}O_4$@Sn-MOF (1:1, 1:2, and 1:3) precursors were placed on a quartz boat and passed into a tubular furnace. Then, they were heated up to 700 °C for 2 h, and the resulting black samples were denoted as LFSC-1, LFSC-2, and LFSC-3 respectively.

2.5. Characterization

The phase structures of the samples were investigated by powder X-ray diffraction (XRD) with Cu Kα radiation (Bruker D8). The chemical bonds and elemental composition were explored using X-ray photoelectron spectroscopy (XPS; Thermo Scientific K-Alpha). The micromorphology and structure of the samples were examined via scanning electron microscopy (SEM; FEI SEM450). The elemental distribution was analyzed using transmission electron microscopy (TEM; Talos F200X), high-resolution TEM (HRTEM), and energy dispersive X-ray spectroscopy (EDS). The electromagnetic parameters were tested with a vector network analyzer (Agilent N5224A). The samples were mixed with paraffin of the same quality and demolded into a coaxial ring (Φ_{out}: 7.0 mm, Φ_{in}: 3.04 mm).

3. Results and discussion

Fe_3O_4 is considered to be a promising candidate for EMWA application due to its low coercivity, high saturation magnetization, and formation of unique electronic channels between Fe^{3+} and Fe^{2+} [13,14]. In this work, the doping of La^{3+} further improves the magnetic loss capability through lattice distortion and orbital coupling [15,16]. However, due to its low electrical conductivity and weak dielectric loss, the EMWA performance of $La_{0.03}Fe_{2.97}O_4$ cannot be further improved. Therefore, CTAB is used as a surfactant to anchor active functional groups on the surface of $La_{0.03}Fe_{2.97}O_4$ for the in-situ growth of stick-shaped Sn-MOF. After calcination, a series of $La_{0.03}Fe_{2.97}O_4/SnO_2$/C (LFSC) samples with good impedance matching and strong EMW attenuation ability are obtained. Fig. 1 shows the specific experimental steps for the preparation of LFSC.

The composition and the phase structure of the synthesized samples were tested via XRD, and the results are shown in Fig. 2a–b. The samples display characteristic diffraction peaks at 30.1°, 35.4°, 43.0°, 53.4°, 56.9°, and 62.5°, corresponding to the (220), (401), (400), (422), (511), and (440) diffraction planes of Fe_3O_4, respectively, verifying the successful synthesis of Fe_3O_4. Furthermore, a significant shift in the (311) peak can be observed in the magnified view (Fig. S1a), which is caused by the fact that the radius of La^{3+} (103 p.m.) is larger than that of Fe^{3+} (65 p.m.) and Fe^{2+} (78 p.m.). The shift in the (311) peak position confirms the successful doping of La^{3+} in Fe_3O_4 [17,18]. Furthermore, all the diffraction peak positions of the synthesized Sn-MOF are in complete agreement with those in the Cambridge Crystal Data Center (CCDC) crystal library No. 785324, demonstrating the successful preparation of Sn-MOF. After calcination, in addition to the characteristic peaks of $La_{0.03}Fe_{2.97}O_4$, the composites also exhibit peaks at 31.8°, 36.8°, 41.4°, 45.6°, 53.1°, 63.3°, and 66.4°, corresponding to the (111), (200), (210), (112), (220), (311), and (222) crystal planes of SnO_2 (PDF#20–1429), respectively. Notably, the diffraction peak corresponding to the (111) crystal plane of LFSC-3 is higher than that of LFSC-1 and LFSC-2, indicating that $La_{0.03}Fe_{2.97}O_4$ is more heavily coated with SnO_2.

The surface elemental valence states of LFSC-2 were characterized using XPS. In the XPS full spectrum (Fig. 2c), it is evident that the LFSC-2 sample contains five elements: C, O, Sn, Fe, and La. The high-resolution

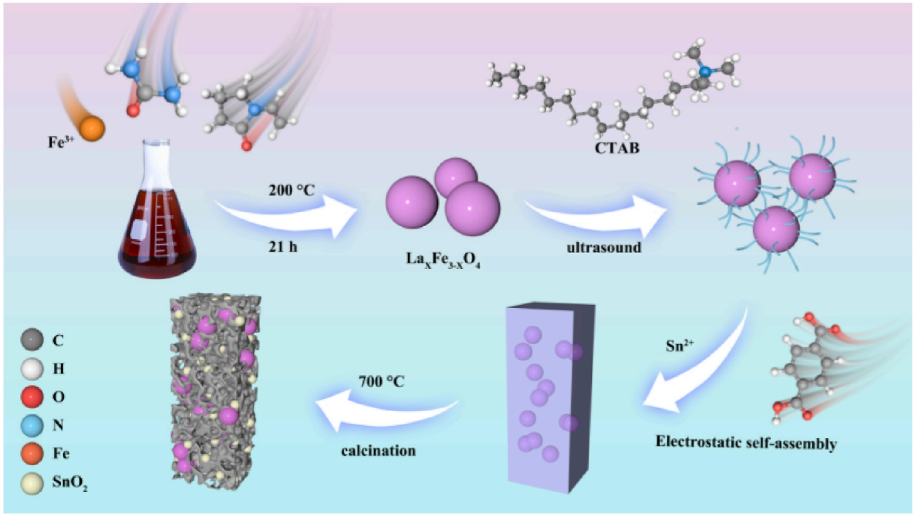

Fig. 1. Schematic diagram of LFSC fabrication process.

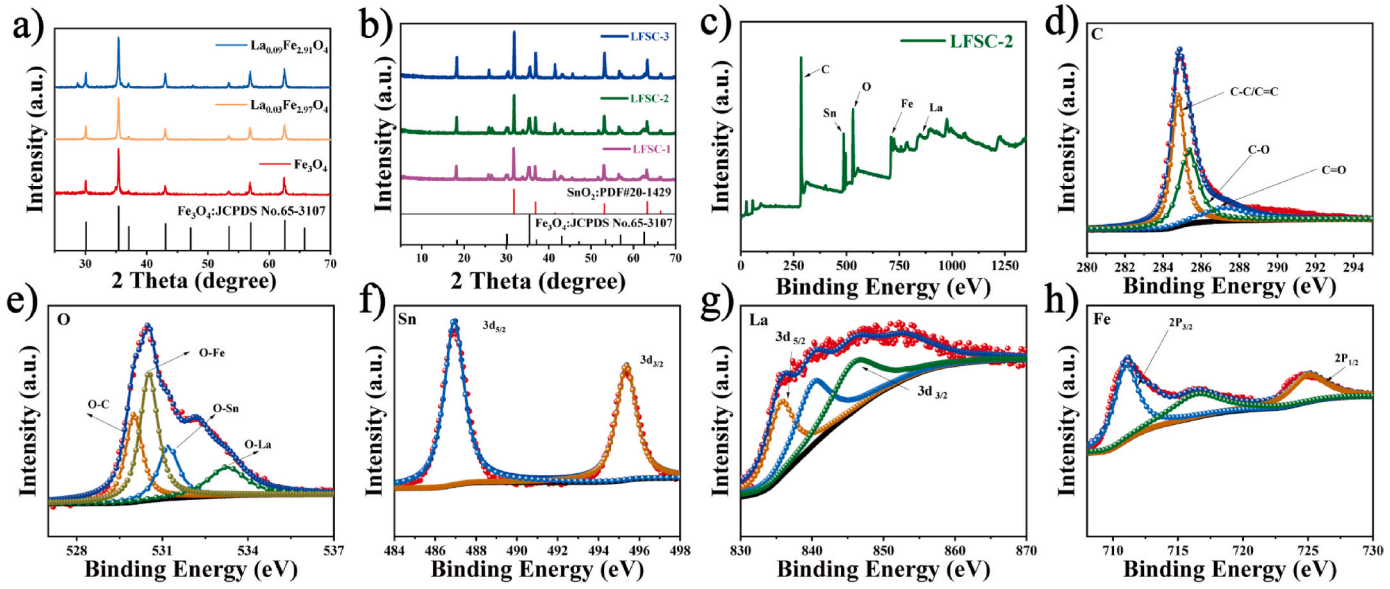

Fig. 2. XRD patterns of (a) $La_xFe_{3-x}O_4$ and (b) LFSC. (c–h) XPS spectra and high-resolution spectra of LFSC.

C 1s spectrum in Fig. 2d shows three characteristic peaks around 289.2, 287.2, and 284.8 eV, corresponding to the O═C–O, C–O, and C–C/C═C bonds, respectively. Fig. 2e shows the O 1s spectrum with multiple peaks at approximately 530.1, 531.5, 533.1, and 532.2 eV, which are attributed to O–C, O–Fe, O–Sn, and O–La bonds, respectively, confirming the presence of $La_{0.03}Fe_{2.97}O_4$ and SnO_2. The characteristic peaks at 486.9 and 485.3 eV in Fig. 2f correspond to Sn $3d_{5/2}$ and $3d_{3/2}$ orbitals, respectively, which further proves the successful synthesis of SnO_2. The peaks at 717.8 and 722.1 eV in Fig. 2g are ascribed to the Fe $2p_{3/2}$ and Fe $2p_{1/2}$ orbitals, respectively. Meanwhile, the peaks at 834.4 and 838.4 eV correspond to the La $3d_{5/2}$ and La $3d_{3/2}$ orbitals, respectively, further demonstrating the doping of La^{3+} in Fe_3O_4.

Fig. S2 and Fig. 3 show the microstructure and morphology of $La_xFe_{3-x}O_4$, Sn-MOF, and LFSC samples. It can be seen in Fig. S2 that $La_xFe_{3-x}O_4$ has a regular spherical structure with a size of approximately 40 nm. Notably, the doping of La^{3+} does not have a significant impact on the micro-morphology. Fig. 3a–c shows the Sn-MOF particles with stick-like structure stacked together, which facilitates multiple reflection and scattering of EMWs. Fig. 3d–l shows the microstructure and morphology of the LFSC samples, and the spherical particles become fully encapsulated with the increase in the proportion of Sn-MOF. This is because the stacked Sn-MOF particles interconnect with each other at high temperatures during the calcination process to form a large carbon network [19,20]. Remarkably, the spherical $La_{0.03}Fe_{2.97}O_4$ and SnO_2 are wrapped by porous carbon, which facilitates the formation of rich interfaces and prevents the oxidation of Fe^{2+}.

TEM was used to investigate the morphology and elemental composition of LFSC-2. As shown in Fig. 4, the spherical $La_{0.03}Fe_{2.97}O_4$ and SnO_2 are wrapped by the carbon layer. In the HRTEM images, the lattice spacings of 0.237 and 0.257 nm clearly correspond to the (200) crystal plane of SnO_2 and (311) crystal plane of Fe_3O_4, respectively [21, 22]. EDS was used to obtain the elemental distribution images of the LFSC-2 composite. The similar distributions of Fe, La, Sn, and O elements, with a weaker signal of La, indicate that the scanned portion is mainly composed of $La_{0.03}Fe_{2.97}O_4$, and SnO_2. Besides, the carbon element is distributed outside the spherical particles, which proves the successful construction of the core-shell heterostructure. The above results are consistent with the XRD and XPS analysis, further confirming the successful synthesis of LFSC-2.

The EMWA performance mainly depends on the values of complex

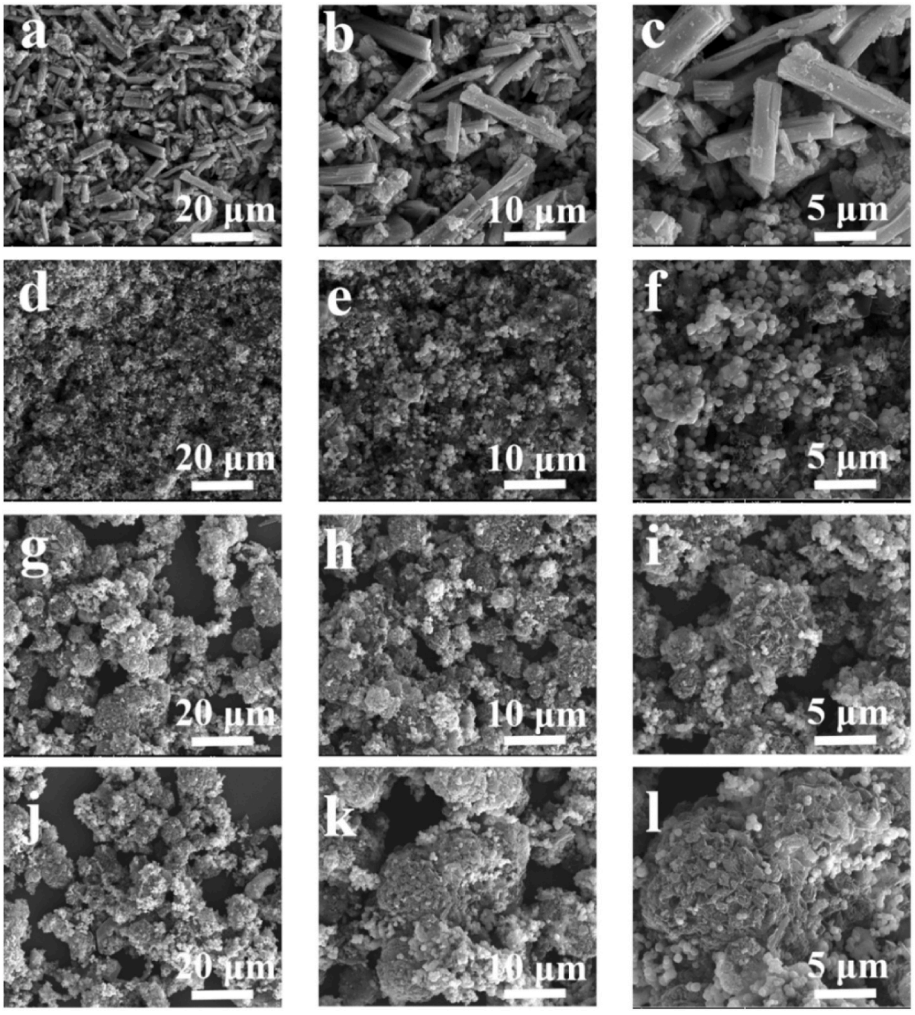

Fig. 3. SEM images of (a–c) Sn-MOF; (d–f) LFSC-1; (g–i) LFSC-2; (j–l) LFSC-3.

permittivity ($\varepsilon_r = \varepsilon' - j\varepsilon''$) and complex permeability ($\mu_r = \mu' - j\mu''$). The real part of permittivity (ε') and permeability (μ') represent the storage ability of electrical and magnetic energy, respectively [23–25]. The imaginary parts (ε'' and μ'') represent the loss ability of electrical and magnetic energy, respectively. As shown in Fig. 5a–d, the permittivity of Fe_3O_4 exhibits an upward trend, which is attributed to the charge hysteresis phenomenon generated by Fe_3O_4 at high frequency. After La^{3+} doping, the ε' values of $La_{0.03}Fe_{2.97}O_4$ slightly increase due to lattice deformation. Further, the ε' values of the material are improved by the introduction of porous carbon derived from Sn-MOF. By analyzing the electromagnetic parameter curve, it can be seen that the ε_r values of LFSC decrease with the increase in frequency due to the frequency dispersion effect [26,27]. Moreover, it is evident that the μ_r values of the $La_xFe_{3-x}O_4$ samples increase with the increase in the doping amount of La^{3+}, demonstrating that the 3d-4f orbital coupling enhances the magnetic loss [28,29]. In addition, when the intrinsic magnetic losses do not fully offset the high-frequency magnetic energy radiation, the values of μ'' can become negative [30].

For an excellent EMWA material, it is not only necessary to achieve an excellent impedance matching (Z) to allow the EMWs to enter the material but also to have a high attenuation constant (α) to dissipate EMWs [31–33]. The values of α and Z are calculated as follows:

$$\alpha = \frac{\sqrt{2}}{c}\pi f \times \sqrt{(\mu''\varepsilon'' - \mu'\varepsilon') + \sqrt{(\mu''\varepsilon'' - \mu'\varepsilon')^2 + (\mu'\varepsilon'' + \mu''\varepsilon')^2}} \quad (1)$$

$$Z = \frac{Z_{in}}{Z_0} \quad (2)$$

Fig. 5e–g shows the two-dimensional (2D) distribution of the impedance matching values at 2–18 GHz under a thickness of 1–5 mm, where the green region (0.8–1.2) indicates better impedance matching. Specifically, LFSC-1 exhibits inadequate EMWA properties, as evidenced by the green region being concentrated at high frequencies and high matching thicknesses. The LFSC-2 and LFSC-3 samples exhibit a broader green region at lower matching thicknesses of 1.5–2.5 mm. Regarding the α values (Fig. 5h), LFSC-1 has the smallest α value, while LFSC-2 shows the highest α value. These results contribute to the optimal EMWA performance of LFSC-2.

Based on the transmission line theory, the EMWA performance of the samples is simulated using the following formulas [34,35]:

$$RL = 20\lg\left|\frac{Z_{in} - Z_0}{Z_{in} + Z_0}\right| \quad (3)$$

$$\left\{Z_0 = \sqrt{\frac{\mu_0}{\varepsilon_0}} \quad Z_{in} = \sqrt{\frac{\mu_r}{\varepsilon_r}}\tan h\left(j\frac{2\pi fd}{c}\sqrt{\mu_r\varepsilon_r}\right)\right\} \quad (4)$$

Here, Z_0 and Z_{in} represent the free space impedance and input impedance, respectively. d, c, and f are thickness, optical velocity, and frequency, respectively. According to Fig. 6, among the $La_xFe_{3-x}O_4$ (x = 0, 0.03, 0.09) samples, $La_{0.03}Fe_{2.97}O_4$ exhibits the best performance with an RL_{min} of −13 dB at 12.6 GHz. This is attributed to the addition of an

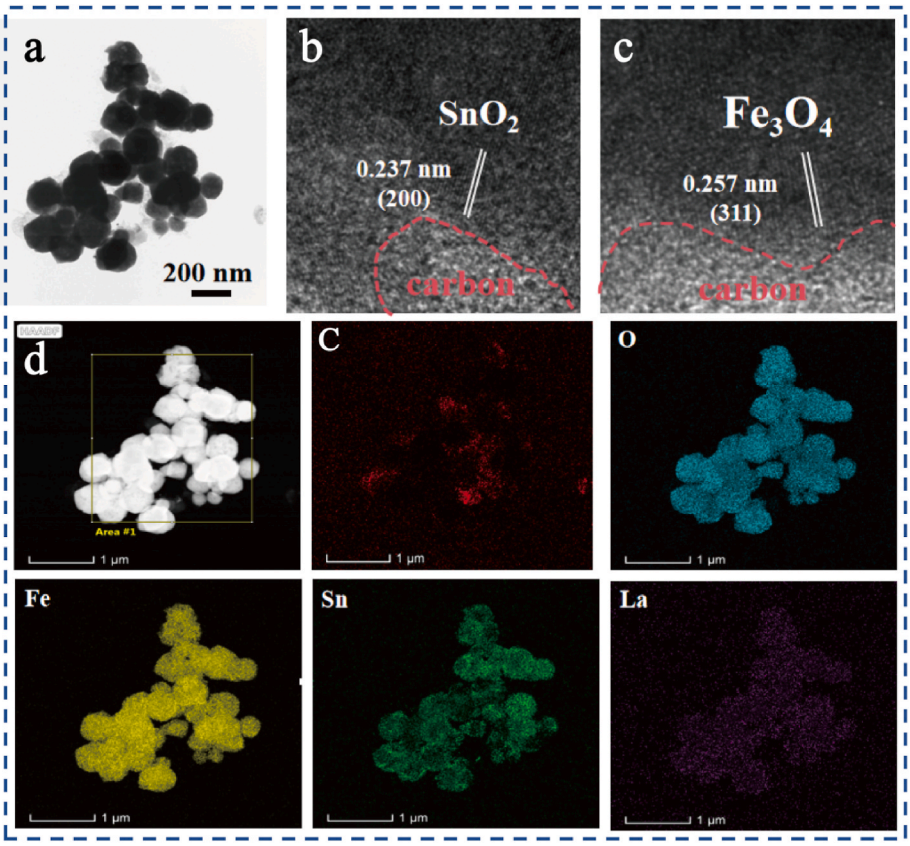

Fig. 4. (a)TEM, (b–c) HRTEM, and (d) EDS elemental mapping images of LFSC-2.

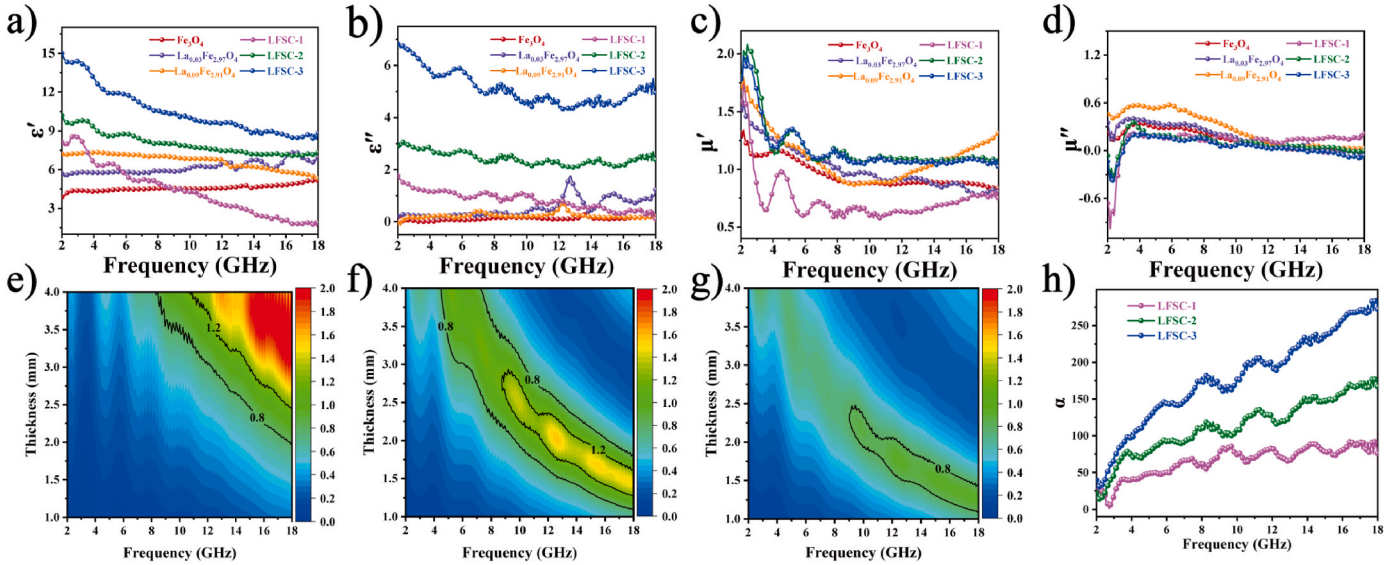

Fig. 5. (a–b) Permittivity and (c–d) permeability of Fe_3O_4,$La_{0.03}Fe_{0.297}O_4$, $La_{0.09}Fe_{0.291}O_4$, LFSC-1, LFSC-2, and LFSC-3. 2D distribution of the impedance matching values for (e) LFSC-1, (f) LFSC-2, and (g) LFSC-3; (h) attenuation ability of LFSC samples.

appropriate amount of La^{3+}, which increases the magnetic loss. After $La_{0.03}Fe_{2.97}O_4$ is encapsulated with Sn-MOF, the introduction of carbon conductive network greatly increases the conductive loss, and the abundant heterojunctions further enhance the interfacial polarization. The RL_{min} and *EAB* of LFSC-2 are −44.1 dB and 3.68 GHz, indicating a strong absorption performance. Meanwhile, the *EAB* and RL_{min} of LFSC-3 are 4.36 GHz and −23.4 dB at a thickness of 1.9 mm, respectively. Fig. 5 indicates that LFSC-3 retains a high ε'', contributing to its excellent EMWA performance at low thickness.

Furthermore, the dielectric loss tangent ($\tan\delta_\varepsilon = \varepsilon''/\varepsilon'$) and magnetic loss tangent ($\tan\delta_\mu = \mu''/\mu'$) are used to quantify the dielectric and magnetic loss abilities, respectively [36,37]. It can be seen in Fig. 7a–b that the $\tan\delta_\varepsilon$ values of LFSC-1 are smaller than its $\tan\delta_\mu$, and the $\tan\delta_\varepsilon$ values of both LFSC-2 and LFSC-3 samples are larger than their $\tan\delta_\mu$ values. These results indicate that the magnetic loss dominates in LFSC-1, while the dielectric loss capacity plays a more significant role in

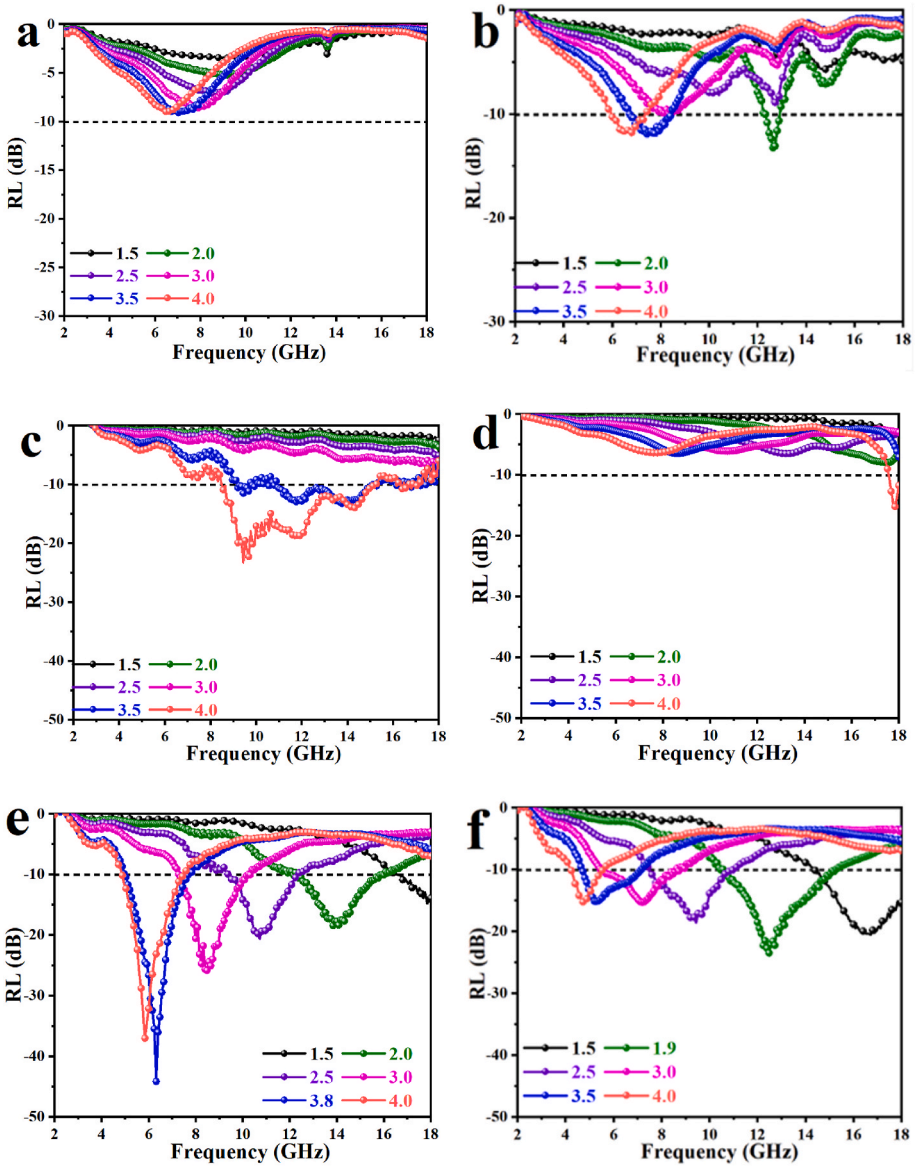

Fig. 6. RL values for (a) Fe_3O_4, (b) $La_{0.03}Fe_{2.97}O_4$, (c) $La_{0.09}Fe_{2.91}O_4$, (d) LFSC-1, (e) LFSC-2, and (f) LFSC-3 at different matching thicknesses and frequencies.

the LFSC-2 and LFSC-3 samples. As the content of Sn-MOF derivative increases, the ε_r and $\tan\delta_\varepsilon$ values of the samples increase. Due to its low dielectric loss capability, LFSC-1 exhibits poor EMWA properties. By contrast, the presence of larger carbon conductive networks in the LFSC-2 and LFSC-3 samples greatly enhances their EWMA properties. As shown in Fig. S3, the *RL* peak frequency (f_m) shifts to lower values with the increase in the absorption layer thickness (t_m), which can be explained by the $\lambda/4$ cancellation theory [38,39]: $t_m = nc/\left(4f_m\sqrt{|\mu_r||\varepsilon_r|}\right)$.

To analyze the polarization relaxation behavior of the samples, the Cole-Cole curves of LFSC-2 and LFSC-3 are shown in Fig. 7c–d. These curves are obtained according to the Debye theory, characterized by the following equations [40,41]:

$$\varepsilon' = \varepsilon_\infty + \frac{\varepsilon_s - \varepsilon_\infty}{1 + (\omega\tau)^2} \tag{5}$$

$$\varepsilon'' = \varepsilon_p'' + \varepsilon_c'' = \frac{\omega\tau(\varepsilon_s - \varepsilon_\infty)}{1 + \omega^2\tau^2} + \frac{\sigma}{\omega\varepsilon_0} \tag{6}$$

$$\left(\varepsilon' - \frac{\varepsilon_s + \varepsilon_\infty}{2}\right)^2 + (\varepsilon'')^2 = \left(\frac{\varepsilon_s - \varepsilon_\infty}{2}\right)^2 \tag{7}$$

where ε_s, ε_0, and ε_∞ represent the vacuum static dielectric constant, dielectric constant, and infinite frequency dielectric constant, respectively; σ and ω are the conductivity and angular frequency, respectively, and τ is the polarization relaxation time. In the Cole-Cole curve, each semicircle illustrates the polarization relaxation behavior, while the upward "tail" is related to conduction loss. As shown in Fig. 7c–d, LFSC-2 and LFSC-3 exhibit multiple polarization relaxation processes, primarily due to abundant interfaces and dipole polarization. Based on equations (4) and (5), the conductive and polarization losses of the samples are further investigated. As depicted in Fig. 7e–f, with the increase in the amount of Sn-MOF, the polarization loss (ε_p'') and conductive loss (ε_c'') of the material significantly increase, which indicates that the introduction of porous carbon and SnO_2 can greatly enhance the heterointerfaces and strengthen the conductive network. Further, the calcination of more Sn-MOF results in the formation of additional microcapacitive heterostructures, which significantly increases the heterogeneous interfaces and improves the polarization loss. Thus, the LFSC-3 sample exhibits the highest polarization loss, which is consistent with the largest number of

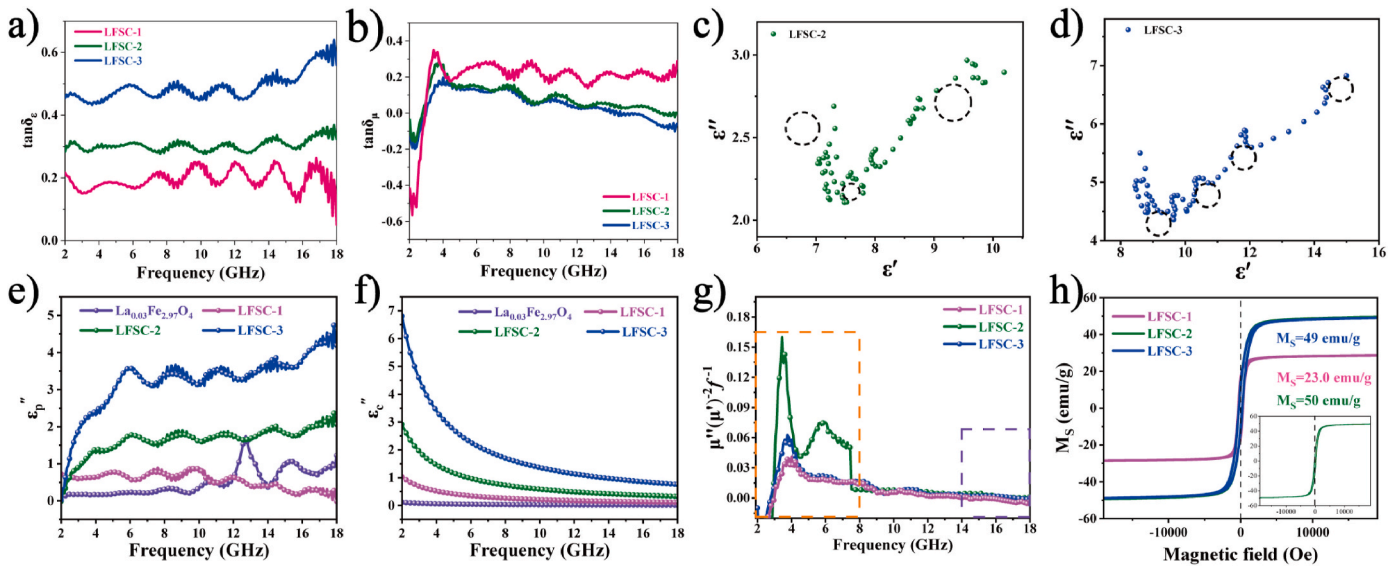

Fig. 7. (a) *tanδ*$_\varepsilon$ and (b) tanδ_μ of the samples. (c–d) Cole-Cole plots (ε'' vs. ε') of LFSC-2 and LFSC-3. (e–f) Polarization and conductive losses of samples. (g) C_0 *and* (h) magnetic saturation intensities of LFSC samples.

Cole-Cole semi-circles. At low frequencies, the conductive loss predominates over polarization loss, while at high frequencies, the polarization loss becomes dominant. Comparing the full XPS spectra of LFSC-2 and LFSC-3 in Fig. S4, it can be seen that the Sn content increases from 0.72 in LFSC-2 to 2.99 in LFSC-3, and the O content rises from 18.83 to 22.54. This indicates a higher generation of SnO_2 in the sample, promoting the formation of abundant heterogeneous interfaces, resulting in more Cole-Cole semi-circles. At the same time, SnO_2 with semiconducting properties enhances the conductive loss. In summary, the increase in Sn content further confirms that LFSC-3 has more Cole-Cole semicircles, with enhanced conductive loss and polarization loss capability.

The eddy current coefficient (C_0) is shown in Fig. 7g [42,43]. The smooth C_0 curve from 8 to 14 GHz indicates the presence of eddy current loss. The carbon wrapping the magnetic particles and further interacting with SnO_2 avoid the agglomeration of $La_{0.03}Fe_{2.97}O_4$ and suppress the eddy current. The skin effect is effectively inhibited, thereby enhancing the magnetic function of the isolated $La_{0.03}Fe_{2.97}O_4$. The drastic fluctuations in C_0 values at 2–8 GHz and 14–18 GHz suggest the occurrence of natural resonance and exchange resonance phenomena, attributed to the inhomogeneous distribution of magnetic particles in the porous material. The hysteresis curves in Fig. 7h show that the magnetic saturation values of LFSC-1, LFSC-2, and LFSC-3 samples are 23, 50, and 49 emu·g^{-1}, respectively. This phenomenon is ascribed to the fact that the appropriate encapsulation of Sn-MOF effectively separates the $La_{0.03}Fe_{2.97}O_4$ particles, greatly enhancing the magnetic saturation of the materials. However, in LFSC-3, although the introduction of more Sn-MOF can reduce the agglomeration to a great extent, the relative content of $La_{0.03}Fe_{2.97}O_4$ considerably decreases, leading to a slight decline in the magnetic saturation. Thus, the magnetic loss caused by eddy currents and ferromagnetic resonance can significantly impact the EMWA performance of the materials.

Based on the above analysis, the EMWA mechanisms of LFSC are illustrated in Fig. 8. Firstly, the rich porous structure derived from stick-like Sn-MOF allows more EMWs to enter the material, facilitating multiple reflections and scattering, which are beneficial for EMW attenuation. Secondly, after carbonization, the $La_{0.03}Fe_{2.97}O_4$@Sn-MOF-derived heterostructures embedded with $La_{0.03}Fe_{2.97}O_4$ and SnO_2 particles form a large conductive network. This network enables electron movement under varying electromagnetic field, generating microcurrents, as evidenced by the "tails" in the Cole-Cole curves. In addition, the interfacial polarization among $La_{0.03}Fe_{2.97}O_4$, SnO_2, and the carbon network contributes to EMW attenuation, as indicated by the distinct lattice boundaries in the HRTEM image (Fig. 4). Besides, during high-

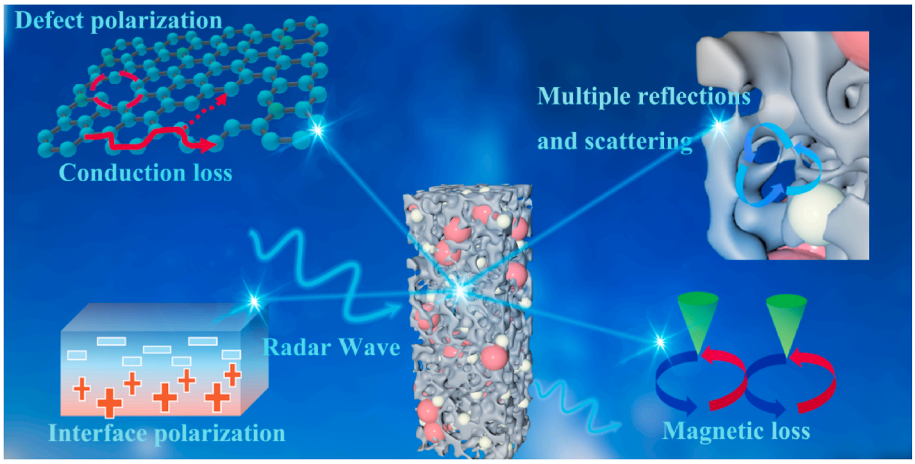

Fig. 8. EMWA mechanisms of LFSC heterostructure.

temperature pyrolysis, significant defects are formed in LFSC, which leads to asymmetric charge distribution and the creation of more polarization centers, thereby enhancing defective polarization. More importantly, $La_{0.03}Fe_{2.97}O_4$, as a Fe_3O_4-based material, benefits from La^{3+} doping, which facilitates the coupling of 3d-4f electron orbitals and enhances the exchange coupling effect between Fe^{2+} and Fe^{3+} ions, substantially increasing the magnetic loss. Notably, natural resonance, exchange resonance, and eddy current loss occur at different frequencies, and the rich magnetic loss greatly increases the EMWA performance.

Fig. S5 analyzes the intrinsic relationships between polarization, conduction, and magnetic losses [44,45]. For $La_{0.03}Fe_{2.97}O_4$, the polarization loss is primarily concentrated in the high-frequency region of 15–18 GHz, which is due to the lattice distortion caused by La doping. Since the internal $La_{0.03}Fe_{2.97}O_4$ and LFSC-1 do not form a complete conductive network, the conductive loss represents a minimal portion of the overall loss. On the other hand, the magnetic loss predominantly occurs in the low- and mid-frequency region of 2–10 GHz, which is attributed to natural resonance effects. Thus, the internal losses in $La_{0.03}Fe_{2.97}O_4$ and LFSC-1 are mainly due to lattice defects and natural resonances.

By contrast, for LFSC-2 and LFSC-3, the interface loss prevails in the high-frequency region, which is attributed to the formation of abundant heterogeneous interfaces between porous carbon, SnO_2, and $La_{0.03}Fe_{2.97}O_4$ within the material. Similarly, the conductive network formed by the porous carbon and SnO_2 dominates the low-frequency region, while the dielectric loss influences the entire frequency band. To summarize, the LFSC samples exhibit excellent EMWA performance due to their unique core-shell structure and the synergistic effects of multiple loss mechanisms.

To significantly optimize the absorption bandwidth, a unique gradient metamaterial structure was designed. This gradient structure facilitates multiple quarter-wavelength diffractions and achieves several absorption peaks in the frequency band, resulting in an ultra-broadband EMWA (Fig. 9a). Specifically, the metamaterial designed based on LFSC-3 achieves ultra-broad *EAB* of 13.17 GHz (4.83–18 GHz), covering 74 % of entire frequency band, making it well suited for practical application. At 5.42 GHz, the electric field is predominantly distributed at the top, while the magnetic field is concentrated at the bottom, with a phase difference close to π/2. This suggests the formation of standing waves inside the material, indicating that EMW interference dominates at this frequency.

To assess the radar stealth performance, the radar cross section (RCS) values of the samples coated on a perfect insulated conductor (PEC) were determined using computer simulation technique (CST) software according to equation S1, [46]. In these simulations, a square PEC model

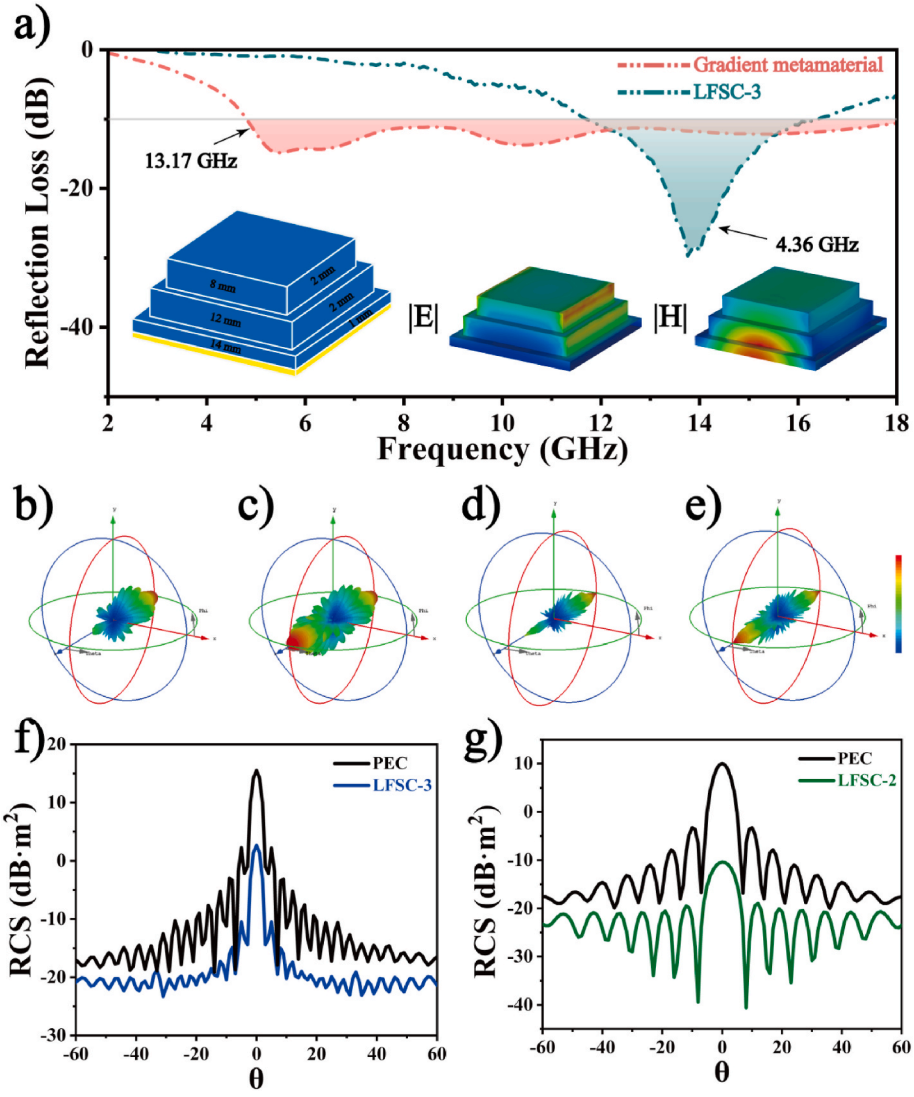

Fig. 9. (a) Gradient structure design of LFSC-3. (b–e) 3D plot of RCS values. (f–g) RCS values of the samples at different angles.

(20×20 cm^2) was coated with LFSC-2 of 3.8-mm thickness or LFSC-3 sample of 1.9-mm thickness. The models were placed on the XY plane and then irradiated with parallel EMWs at frequencies of 6.3 and 12.4 GHz, respectively. The three-dimensional (3D) simulation results (Fig. 9b–e) indicate that the RCS values of the PEC-coated model are all consistently higher than those of the sample-coated models, indicating the strong radar wave absorption capability of all the samples, affirming their potential for radar stealth application.

The angle (θ) between the z-axis and EMWs was varied from −60° to 60° to determine the RCS values at different angles. Fig. 9f–g shows that when θ is 0°, the structural effect can be neglected. In this case, the RCS reduction value of LFSC-3 is 12.9 dB•m^2. By contrast, LFSC-2 exhibits an RCS reduction value of 20.4 dB·m^2, demonstrating superior radar stealth performance compared to LFSC-3.

4. Conclusions

In this study, a novel approach was proposed to enhance the EMWA performance of conventional magnetic materials through in-situ growth of stick-shaped Sn-MOF on La^{3+}-doped Fe_3O_4. La^{3+} doping can greatly promote the magnetic performance of Fe_3O_4 due to 3d-4f orbital coupling and the enhanced exchange coupling effect between Fe^{2+} and Fe^{3+} ions. The core-shell heterostructure of the LFSC composites was successfully constructed by using CTAB as a bridging link. The porous structure of LFSC optimized the impedance matching and facilitated multiple reflections and scattering of EMWs. $La_{0.03}Fe_{2.97}O_4$ and SnO_2 microspheres were embedded within the carbon matrix, which boosted the attenuation of EMWs through mechanisms such as conductive loss, interfacial polarization, and magnetic loss. Because of the electromagnetic synergistic enhancement effect, LFSC-2 exhibited strong EMWA performance, with an RL_{min} of −44.1 dB. Meanwhile, the metamaterial designed based on LFSC-3 exhibited an *EAB* of 13.17 GHz, highlighting its potential applicability over a wide frequency range. Moreover, the RCS simulation results confirmed the strong radar stealth capability of LFSC. Overall, based on La^{3+} doping and a tailored structural design, the proposed LFSC materials offer promising advancements in EMWA application and radar stealth technology.

CRediT authorship contribution statement

Huiliang Wen: Project administration, Methodology, Investigation, Conceptualization. **Wei Xu:** Writing – review & editing, Formal analysis, Data curation. **Sen Lin:** Validation, Investigation. **Aiguo Guan:** Writing – review & editing, Supervision, Data curation. **Yingna Zhang:** Resources, Investigation, Formal analysis, Data curation. **Xin Li:** Writing – original draft, Software. **Chongbo Liu:** Writing – review & editing, Supervision, Funding acquisition.

Declaration of competing interest

The authors declare that they have no known competing financial interests or personal relationships that could have appeared to influence the work reported in this paper.

Acknowledgements

This work was supported by the National Natural Science Foundation of China (22265021) and the Aeronautical Science Foundation of China (2020Z056056003). The authors would like to thank Shiyanjia Lab (https://www.shiyanjia.com) for XPS analysis and MJEditor (https://www.mjeditor) for its linguistic assistance during the preparation of this manuscript.

Appendix A. Supplementary data

Supplementary data to this article can be found online at https://doi.org/10.1016/j.carbon.2024.119613.

References

[1] X. Li, R.Z. Hu, Z.Q. Xiong, D. Wang, Z.X. Zhang, C.B. Liu, et al., Metal-organic gel leading to customized magnetic-coupling engineering in carbon aerogels for excellent radar stealth and thermal insulation performances, Nano-Micro Lett. 16 (2024) 42.
[2] J.J. Li, D. Lan, Y.H. Cheng, Z.R. Jia, P.B. Liu, X.T. Shi, et al., Constructing mixed-dimensional lightweight magnetic cobalt-based composites heterostructures: an effective strategy to achieve boosted microwave absorption and self-anticorrosion, J. Mater. Sci. Technol. 196 (2024) 60–70.
[3] Z.G. Gao, D. Lan, X.Y. Ren, Z.R. Jia, G.L. Wu, Manipulating cellulose-based dual-network coordination for enhanced electromagnetic wave absorption in magnetic porous carbon nanocomposites, Compos. Commun. 48 (2024) 101922.
[4] X.L. Chen, D. Lan, L.T. Zhou, Z. Zeng, Y.K. Liu, S.X. Du, et al., Rational construction of ZnFe2O4 decorated hollow carbon cloth towards effective electromagnetic wave absorption, Ceram. Int. 50 (2024) 24549–24557.
[5] L.X. Wang, Y.K. Guan, X. Qiu, H.L. Zhu, S.B. Pan, M.X. Yu, et al., Efficient ferrite/Co/porous carbon microwave absorbing material based on ferrite@metal-organic framework, Chem. Eng. J. 326 (2017) 945–955.
[6] Z. Ma, K. Yang, D. Li, H. Liu, S. Hui, Y. Jiang, et al., The electron migration polarization boosting electromagnetic wave absorption based on Ce atoms modulated yolk@ shell FexN@ NGC, Adv. Mater. (2024) 2314233.
[7] W.H. Gu, J.Q. Sheng, Q.Q. Huang, G.H. Wang, J.B. Chen, G.B. Ji, Environmentally friendly and multifunctional Shaddock peel-based carbon aerogel for thermal-insulation and microwave absorption, Nano-Micro Lett. 13 (2021) 102.
[8] C.B. Liu, X.L. Nie, H.L. Wen, Diaquabis (5-carboxy-2-methyl-1H-imidazole-4-carboxylato-κ^{2}N^3,O^4) cobalt (II), Acta Cryst. 63 (2007) 2244.
[9] C.B. Liu, Y.N. Gong, Y. Chen, H.L. Wen, Self-assembly and structures of new transition metal complexes with phenyl substituted pyrazole carboxylic acid and N-donor co-ligands, Inorg. Chim. Acta. 383 (2012) 277–286.
[10] Y. Chen, C.B. Liu, Y.N. Gong, J.M. Zhong, H.L. Wen, Syntheses, crystal structures and antibacterial activities of six cobalt(II) pyrazole carboxylate complexes with helical character, Polyhedron 36 (2012) 6–14.
[11] B. Liu, B. Liang, J. Xiao, M. Feng, H. Cheng, et al., MOF derived NiFe@ C composites with controllable multi-dimensional microstructures for broadband microwave absorption, Compos. Part A 176 (2024) 107869.
[12] B. Zhao, G. Shao, B.B. Fan, W.H. Guo, Y.Q. Chen, R. Zhang, Preparation of SnO_2-coated Ni microsphere composites with controlled microwave absorption properties, Appl. Surf. Sci. 332 (2015) 112–120.
[13] X. Meng, W.J. Lei, W.W. Yang, Y.Q. Liu, Y.S. Yu, Fe_3O_4 nanoparticles coated with ultra-thin carbon layer for polarization-controlled microwave absorption performance, J. Colloid Interface Sci. 600 (2021) 382–389.
[14] Z. Tong, Z. Liao, Y. Liu, M. Ma, Y. Bi, W. Huang, et al., Hierarchical Fe_3O_4/Fe@C@MoS_2 core-shell nanofibers for efficient microwave absorption, Carbon 179 (2021) 646–654.
[15] X. Cai, J. Wang, B. Li, A. Wu, B. Xu, B. Wang, et al., Microwave absorption properties of LiZn ferrites hollow microspheres doped with La and Mg by self-reactive quenching technology, J. Alloys Compd. 657 (2016) 608–615.
[16] X. Liu, L. He, G. Han, J. Sheng, Y. Yu, W. Yang, Design of rich defects carbon coated $MnFe_2O_4$/$LaMnO_3$/$LaFeO_3$ heterostructure nanocomposites for broadband electromagnetic wave absorption, Chem. Eng. J. 476 (2023) 146199.
[17] Z. Liu, F. Pan, B. Deng, Z. Xiang, W. Lu, Self-assembled MoS_2/3D worm-like expanded graphite hybrids for high-efficiency microwave absorption, Carbon 174 (2021) 59–69.
[18] J. Yao, J. Zhou, L. Lu, F. Yang, Z. Yao, B. Ouyang, et al., Rare earth lanthanum pinning effect for corrosion resistance ultra-efficient microwave absorption FeCo@rGO composites, J. Mater. Sci. Technol. 177 (2024) 181–190.
[19] R. Qin, A. Ou, Y. Li, H. Deng, Y. Liu, X. Liu, Noticeably enhanced microwave absorption performance via constructing molecular-level interpenetrating carbon network heterostructure, Carbon 183 (2021) 858–871.
[20] X. Xu, F. Ran, Z. Fan, Z. Cheng, T. Lv, L. Shao, et al., Acidified bimetallic MOFs constructed Co/N co-doped low dimensional hybrid carbon networks for high-efficiency microwave absorption, Carbon 171 (2021) 211–220.
[21] Y. Wang, Z. Peng, W. Jiang, Controlled synthesis of Fe_3O_4@SnO_2/RGO nanocomposite for microwave absorption enhancement, Ceram. Int. 42 (2016) 10682–10689.
[22] K.S. Sista, S. Dwarapudi, D. Kumar, G.R. Sinha, A.P. Moon, Carbonyl iron powders as absorption material for microwave interference shielding: a review, J. Alloys Compd. 853 (2021) 157251.
[23] Q.L. Zhang, D. Lan, S.L. Deng, J.W. Gu, Y.Q. Wang, J.W. Ren, et al., Constructing multiple heterogeneous interfaces in one-dimensional carbon fiber materials for superior electromagnetic wave absorption, Carbon 226 (2024) 119223.
[24] H. Zhu, J. Yin, X. Wang, H. Wang, X. Yang, Microorganism-derived heteroatom-doped carbon materials for oxygen reduction and supercapacitors, Adv. Funct. Mater. 23 (2013) 1305–1312.
[25] S. Hu, G. Wu, Z. Huang, X. Chen, Microwave absorption behavior of ZnO whisker modified by nanosized Fe_3O_4 particles, J. Nanosci. Nanotechnol. 10 (2010) 7592–7595.
[26] M.Z. Khan, I.H. Gul, F.A. Tahir, Encapsulation of Ba–Sr hexaferrite nanoparticlesand MWCNTs in conductive polymer matrix for improved dielectric spectroscopy, electromagnetic shielding and microwave absorption applications, Ceram. Int. 49 (2023) 27796–27814.

[27] J. Wang, Z. Wu, Y. Xing, L. Liu, A novel 1D/2D interpenetrating network architecture of MXene/cellulose composite microfiber and graphene for broadband microwave absorption, Chem. Eng. J. 439 (2022) 135734.
[28] R.R. Kanna, S. Jaisiva, N.R. Dhineshbabu, M.P. Kesavan, N. Lenin, L. Guru Prasad, et al., Microwave-absorbing behavior of rare-earth-ion-doped copper manganese nanoferrites in X-band frequency, Ceram. Int. (2024), https://doi.org/10.1016/j.ceramint.2024.07.355.
[29] X. He, Z. Xiong, C. Lei, Z. Shen, A. Ni, Y. Xie, et al., Excellent microwave absorption performance of $LaFeO_3/Fe_3O_4$/C perovskite composites with optimized structure and impedance matching, Carbon 213 (2023) 118200.
[30] F. Pan, X.F. Wu, D. Batalu, W. Lu, H.T. Guan, Assembling of low-dimensional aggregates with interlaminar electromagnetic synergy network for high-efficient microwave absorption, Adv. Powder Mater. 2 (2023) 100100.
[31] H. Wang, S. Feng, M. Sun, X. Li, C. Wang, Z. Lin, et al., Fabrication of hollow core-shell $NiCo_2O_4$@ polypyrrole nanofibers/reduced graphene oxide ternary composites with excellent microwave absorption performances, J. Colloid Interface Sci. 658 (2024) 889–902.
[32] H. Gu, J. Huang, N. Li, H. Yang, G. Chen, C. Dong, et al., Reactive MnO2 template-assisted synthesis of double-shelled PPy hollow nanotubes to boost microwave absorption, J. Mater. Sci. Technol. 146 (2023) 145–153.
[33] Q. Gao, X. Ye, E. He, T. Yan, Y. Wang, C. Huang, et al., 3D printed composites achieve broadband electromagnetic wave absorption by introducing carbon black/carbonyl iron powder porous hollow microspheres, Mater. Sci. Eng. B 299 (2024) 116937.
[34] D. Lan, Y. Hu, M. Wang, Y. Wang, Z.G. Gao, Z.R. Jia, Perspective of electromagnetic wave absorbing materials with continuously tunable effective absorption frequency bands, Compos. Commun. 50 (2024) 101993.
[35] J.X. Zhou, X.M. Huang, D. Lan, Y.H. Cheng, F.Y. Xue, C.Y. Jia, et al., Polymorphic cerium-based Prussian blue derivatives with growing CNT/Co heterojunctions for enhanced microwave absorption via polarization and magnetization, Nano Res. 17 (2023) 2050–2060.
[36] Y. Zhu, J. Zhou, C. Wu, Y. Wang, Y. Liu, Effect of annealing temperature on the magnetic and microwave absorption of FeNi alloy, J. Magn. Magn Mater. 570 (2023) 170535.
[37] H.S. Ahmad, T. Hussain, Y. Nawab, S. Salamat, Effect of various dielectric and magnetic nanofillers on microwave absorption properties of carbon fiber reinforced composites structures, Ceram. Int. 48 (2022) 19882–19890.
[38] B. Wang, J. Wei, Y. Yang, T. Wang, F. Li, Investigation on peak frequency of the microwave absorption for carbonyl iron/epoxy resin composite, J. Magn. Magn Mater. 323 (2011) 1101–1103.
[39] R. Tan, F. Zhou, Y. Liu, B. Zhang, Y. Yang, J. Zhou, et al., 3D printed propeller-like metamaterial for wide-angle and broadband microwave absorption, J. Mater. Sci. Technol. 144 (2023) 45–53.
[40] G.J. Ma, D. Lan, Y. Zhang, X.Y. Sun, Z.R. Jia, G.L. Wu, et al., Microporous cobalt ferrite with bio-carbon loosely decorated to construct multi-functional composite for dye adsorption, anti-bacteria and electromagnetic protection, Small (2024) 2404449.
[41] N.N. Wu, B.B. Zhao, Y.Y. Lian, S.S. Liu, Y. Xian, J.W. Gu, et al., Metal organic frameworks derived Ni_xSe_y@NC hollow microspheres with modifiable composition and broadband microwave attenuation, Carbon 226 (2024) 119215.
[42] L. Meng, J. Li, X. Li, Z. Wang, W. Zhou, Fabrication of core-shell Co@ HCN@ PANI composite material with enhanced electromagnetic wave absorption, J. Alloys Compd. 966 (2023) 171528.
[43] W. Song, Q. Zhao, Z. Wang, Magnetic biomass porous carbon@ Co/CoO nanocomposite for highly efficient microwave absorption, Mater. Res. Bull. 167 (2023) 112371.
[44] Q.Q. Wang, B. Niu, Y.H. Han, Q. Zheng, L. Li, M.S. Cao, Nature-inspired 3D hierarchical structured "vine" for efficient microwave attenuation and electromagnetic energy conversion device, Chem. Eng. J. 452 (2023) 139042.
[45] J.C. Shu, M.S. Cao, M. Zhang, X.X. Wang, W.Q. Cao, X.Y. Fang, et al., Molecular patching engineering to drive energy conversion as efficient and environment-friendly cell toward wireless power transmission, Adv. Funct. Mater. 30 (2020) 1908299.
[46] K. Ran, W. Wang, X. Hou, Y. Huang, Z. Zhang, D. He, et al., Oxygen plasma modulates the interfacial impedance of microwave reduced graphene oxide for enhanced microwave absorption, J. Alloys Compd. 924 (2022) 166568.